

Article

# Multiple Effects of High Surface Area Hollow Nanospheres Assembled by Nickel Cobaltate Nanosheets on Soluble Lithium Polysulfides

Jun Pu <sup>1,2,\*</sup> , Xiaomei Zhu <sup>1</sup>, Jie Wang <sup>3</sup> and Shaomeng Yu <sup>3</sup>

<sup>1</sup> Key Laboratory of Functional Molecular Solids, Ministry of Education, College of Chemistry and Materials Science, Anhui Normal University, Wuhu 241002, China

<sup>2</sup> Anhui Provincial Engineering Laboratory for New-Energy Vehicle Battery Energy-Storage Materials, Anhui Normal University, Wuhu 241002, China

<sup>3</sup> College of Chemistry and Chemical Engineering, Anqing Normal University, Anqing 246000, China

\* Correspondence: [jpu@ahnu.edu.cn](mailto:jpu@ahnu.edu.cn)

**Abstract:** Inhibiting the shuttle effect of soluble polysulfides and improving slow reaction kinetics are key factors for the future development of Li–S batteries. Herein, edelweiss shaped NiCo<sub>2</sub>O<sub>4</sub> hollow nanospheres with a high surface area were prepared by a simple template method to modify the separator to realize multiple physical constraints and strong chemical anchoring on the polysulfides. On one hand, the good electrolyte wettability of NiCo<sub>2</sub>O<sub>4</sub> promoted the migration of Li-ions and greatly improved the dynamics. On the other hand, mesoporous NiCo<sub>2</sub>O<sub>4</sub> nanomaterials provided many strong chemical binding sites for loading sulfur species. The hollow structure also provided a physical barrier to mitigate the sulfur species diffusion. Therefore, the modified separator realized multiple physical constraints and strong chemical anchoring on sulfur species. As a result, the sulfur cathode based on this composite separator showed significantly enhanced electrochemical performance. Even at 4 C, a high capacity of 505 mAh g<sup>-1</sup> was obtained, and about 80.6% could be retained after 300 cycles.

**Keywords:** hollow nanospheres; separator modification; nickel cobaltate; lithium polysulfides



**Citation:** Pu, J.; Zhu, X.; Wang, J.; Yu, S. Multiple Effects of High Surface Area Hollow Nanospheres Assembled by Nickel Cobaltate Nanosheets on Soluble Lithium Polysulfides. *Molecules* **2023**, *28*, 1539. <https://doi.org/10.3390/molecules28041539>

Academic Editor: Shijun Liao

Received: 9 January 2023

Revised: 1 February 2023

Accepted: 3 February 2023

Published: 5 February 2023



**Copyright:** © 2023 by the authors. Licensee MDPI, Basel, Switzerland. This article is an open access article distributed under the terms and conditions of the Creative Commons Attribution (CC BY) license (<https://creativecommons.org/licenses/by/4.0/>).

## 1. Introduction

The lithium–sulfur (Li–S) battery, as a new electrochemical system, has been widely concerned in the market of secondary energy storage. It not only has a rich source of raw materials, but also has ultrahigh theoretical specific capacity (1675 mAh g<sup>-1</sup>) and energy density (2600 Wh kg<sup>-1</sup>), which is several times more than the conventional Li-ion battery with LiCoO<sub>2</sub> or LiFePO<sub>4</sub> as the cathode [1,2]. Unfortunately, the large-scale commercialization of Li–S batteries still faces several challenges such as the poor conductivity of sulfur, dissolution of lithium polysulfides (LiPSs), and slow reaction kinetics [3–6]. Among them, the shuttle effect caused by soluble LiPSs (Li<sub>2</sub>S<sub>n</sub>, 4 ≤ n ≤ 8) can cause an irreversible loss of active material and a rapid decline in capacity [7]. How to solve the shuttle effect is the key to its future development [8].

In principle, the shuttle effect is the diffusion of LiPSs back and forth between the positive and negative electrodes. The separator of the cell is the only channel through which these behaviors of LiPSs occur. If the separator is designed so that it does not allow LiPSs to pass through, the shuttle effect will be fundamentally resolved. Obviously, the commercial polypropylene (PP) separator is not up to this difficult task due to the large-pore framework [9].

In recent years, many studies have shown that the initial PP separator can be modified (separator engineering) to obtain different inhibition abilities of LiPS diffusion [9–11]. Carbon based materials (carbon nanofibers, mesoporous carbon, etc.) were first used to

modify the Li-S separator [12,13]. However, the “non-polar” carbon has a limited effect on the shuttle of LiPSs, because its interaction with the latter is in the category of van der Waals forces [14,15]. The carbon coating with a high specific area on separator is only a barrier layer in the physical sense. The soluble LiPSs will still be shed from the carbon substance during long or high load electrochemical cycles. In addition, carbon materials cannot effectively solve the problem of slow LiPS conversion kinetics. Therefore, transition metal oxides with a “polar surface” are increasingly being studied. It has a good affinity with LiPSs and can effectively anchor the latter. More importantly, some metal oxides have a certain catalytic effect, which can promote the LiPS reaction. Different oxides including  $\text{MnO}_2$ ,  $\text{Fe}_2\text{O}_3$ , and  $\text{NiO}$  are used in Li-S batteries [16–18]. For instance, Wang et al. coated a functional  $\text{MnO}_2$ /graphene oxide/carbon nanotube composite interlayer on a PP separator in Li-S batteries. Combined with the anchoring effect of  $\text{MnO}_2$  on LiPSs and the stability of carbon materials, the modified electrode can effectively inhibit the diffusion of LiPSs [16]. Among these oxides, the ternary metal oxide composed of two different metal cations shows higher electronic conductivity and electrochemical activity than mono-metal oxides due to its complex chemical composition and the synergistic action [19,20]. Unfortunately, the low surface area and heavy block are not conducive to the energy density. It can be seen that the correct design of transition metal oxide as a modified material for a Li-S separator still faces many challenges and is worth exploring.

Herein, the edelweiss shaped nickel cobaltate ( $\text{NiCo}_2\text{O}_4$ ) hollow nanospheres were prepared by a simple template method (Figure 1a). The structure consisted of lots of ultra-thin  $\text{NiCo}_2\text{O}_4$  nanosheets, which showed a specific surface area of up to  $281 \text{ m}^2 \text{ g}^{-1}$ , meaning that it has a more active area as a separator modification material. The high surface area adsorbed more sulfur species and closed them in the inner cavity of  $\text{NiCo}_2\text{O}_4$ , further inhibiting the migration of soluble LiPSs. In addition, the rich Ni-Co sites provided a good catalytic path for the rapid LiPS conversion. Unlike the conventional PP separator cell (Figure 1b), the battery based on such a  $\text{NiCo}_2\text{O}_4$  coated separator (defined as  $\text{NiCo}_2\text{O}_4@\text{PP}$ ) obtained an excellent electrochemical performance (Figure 1c). A high reversibility of  $1386 \text{ mAh g}^{-1}$  could be obtained at 0.2 C. When the current density was increased to 4 C, the capacity was still as high as  $505 \text{ mAh g}^{-1}$  and remained about 80.6% after 300 cycles. Even with a high loading of  $3.16 \text{ mg cm}^{-2}$ , the battery with a modified separator could still achieve a  $\sim 3.2 \text{ mAh cm}^{-2}$  area capacity, which greatly increased its potential to meet the actual requirements.

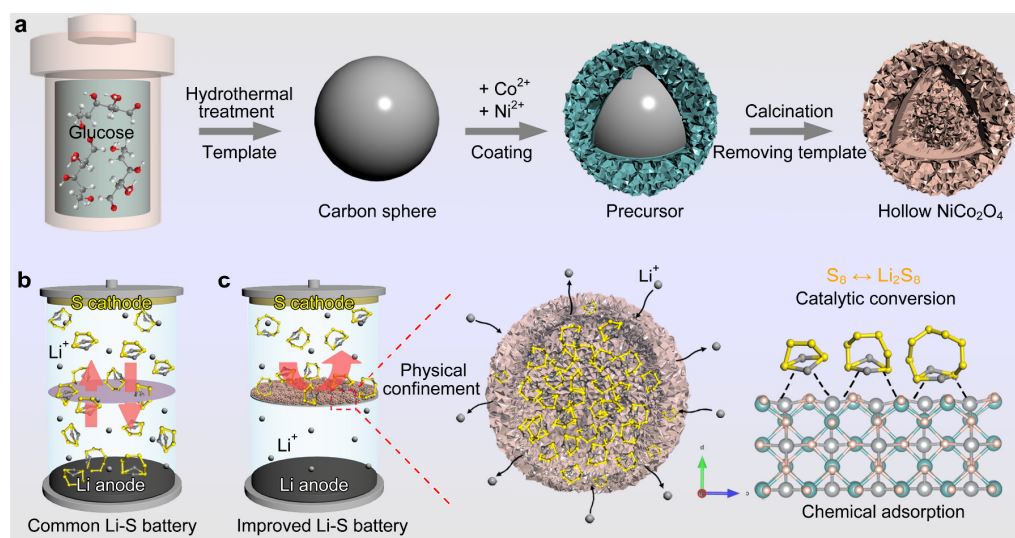


**Figure 1.** Schematic diagrams of (a) the synthesis process of  $\text{NiCo}_2\text{O}_4$  hollow nanospheres, (b) a Li-S battery with a common PP separator, and (c) an improved Li-S system using a  $\text{NiCo}_2\text{O}_4@\text{PP}$  separator for minimizing the issues of LiPSs.

## 2. Results and Discussion

As shown in Figure 1a, the synthesis of the  $\text{NiCo}_2\text{O}_4$  sample went through three stages: template preparation, precursor adsorption and calcination (template removal). Through the classical hydrothermal reaction, the carbon sphere template with a smooth surface and uniform particle size (Figure S1a) was obtained [21]. In the subsequent precursor coating process, Ni and Co ions were firmly adsorbed by various functional groups on the carbon surface, and formed a tight coating layer (Figure S1b). Finally, the calcination in the air not only removed the carbon substrate, but also enabled the precursor on the surface to obtain an abundant pore structure.

The phase and purity of the as-obtained samples were first determined by X-ray powder diffraction (XRD) in Figure 2a. All patterns matched those of spinel  $\text{NiCo}_2\text{O}_4$  (JCPDS No. 20-0781). The diffraction peaks at about  $18.9^\circ$ ,  $31.1^\circ$ ,  $36.7^\circ$ ,  $38.4^\circ$ ,  $44.6^\circ$ ,  $55.4^\circ$ ,  $59.1^\circ$ , and  $64.9^\circ$  corresponded to the (111), (220), (311), (222), (400), (422), (511), and (440) planes, respectively. The absence of other peaks meant that the sample was pure. Meanwhile, combined with the thermogravimetric analysis (TGA) results in Figure S2, it can be inferred that the carbon template is basically removed after a long time of heat treatment in air. Figure 2b depicts the scanning electron microscopy (SEM) image of  $\text{NiCo}_2\text{O}_4$ . Obviously, the samples maintained a spherical shape similar to that of the precursors that were about 400 nm in diameter. From the transmission electron microscopy (TEM) in Figure 2c, it can be seen that the edelweiss shaped nanospheres were hollow structures. The walls of these spheres were made up of a large number of ultra-thin  $\text{NiCo}_2\text{O}_4$  nanosheets. In addition, closer inspection revealed that the nanosheets had a rich pore structure, which would greatly improve the surface area of the materials. Figure S3 shows the SEM and TEM elemental mapping results. Obviously, the Ni, Co, and O elements were continuously and uniformly distributed in the as-prepared hollow  $\text{NiCo}_2\text{O}_4$  sample. This once again proved the purity and image of the  $\text{NiCo}_2\text{O}_4$  sample. The high-resolution TEM (HRTEM) in Figure 2d had the lattice fringes of 0.47 nm and 0.28 nm, which corresponded to the (111) plane and (220) plane of the spinel  $\text{NiCo}_2\text{O}_4$ , respectively.

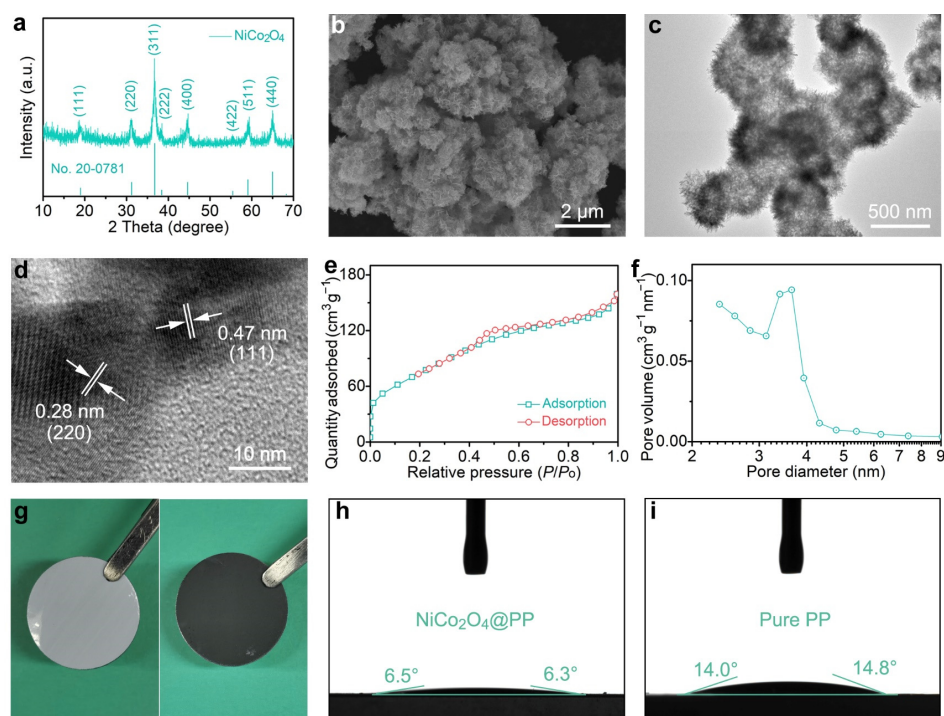


**Figure 2.** (a) XRD, (b) SEM, (c) TEM, and (d) HRTEM characteristics of the as-obtained  $\text{NiCo}_2\text{O}_4$  sample. (e,f)  $\text{N}_2$  adsorption–desorption isotherm and pore size distribution. (g) Photographs of the  $\text{NiCo}_2\text{O}_4$ @PP separator. (h,i) Contact angle tests of the modified and pure separators.

The Brunauer–Emmett–Teller (BET) surface area of NiCo<sub>2</sub>O<sub>4</sub> was determined by the N<sub>2</sub> adsorption–desorption isotherm, as shown in Figure 2e. A type-IV curve with a pronounced hysteresis loop could be observed, indicating the high porosity of the sample [22]. Surprisingly, the BET surface area could be calculated as 281 m<sup>2</sup> g<sup>−1</sup>, which was larger than the NiCo<sub>2</sub>O<sub>4</sub> nanostructures reported in most of the other literature [20,22,23]. This might be due to the abundance of nanopores on the nanosheets. The pore size distribution at about 3.4 nm (Figure 2f) indicated that the sample had good mesoporous properties. In general, an extremely high surface area and abundant pore structure would greatly improve the adsorption site of NiCo<sub>2</sub>O<sub>4</sub> to LiPSs and the infiltration and transfer rate of electrolyte and charge [24,25].

Using the slurry coating method, the fluffy hollow NiCo<sub>2</sub>O<sub>4</sub> nanospheres were uniformly coated on one side of the commercial PP separator. As shown in Figure 2g, the other side of the modified separator remained intact. As a qualified separator modification layer, the composite NiCo<sub>2</sub>O<sub>4</sub>@PP should have a good electrolyte affinity, that is, it should not hinder the diffusion of electrolyte [16,26]. For this purpose, the contact angle experiments of the Li–S electrolyte on different separators were tested (Figure 2j,i). Obviously, the contact angle between the electrolyte and NiCo<sub>2</sub>O<sub>4</sub>@PP sample was ~6.4°. However, for the pure PP separator, the contact angle was as high as ~14.4°, indicating that the prepared NiCo<sub>2</sub>O<sub>4</sub> not only did not hinder the diffusion of the electrolyte, but provided a better infiltrative property, which would be conducive to the kinetic acceleration of the electrochemical system [27].

In order to explore the anchoring effect and mechanism of NiCo<sub>2</sub>O<sub>4</sub> on soluble LiPSs, a series of theoretical calculations and experimental verification were carried out. As shown in Figure 3a, the interaction between the soluble LiPSs (Li<sub>2</sub>S<sub>4</sub>, Li<sub>2</sub>S<sub>6</sub>, and Li<sub>2</sub>S<sub>8</sub>) and NiCo<sub>2</sub>O<sub>4</sub> substrate was obvious, and the corresponding binding energies were 2.88 eV, 3.28 eV, and 3.10 eV, respectively. Importantly, the geometric configuration of these polysulfide molecules on the substrate was stable, indicating that NiCo<sub>2</sub>O<sub>4</sub> was relatively stable for the electrochemical systems and chemical interactions [28,29]. In contrast, the binding energies of LiPSs on the carbon surface were less than 0.6 eV (Figure 3b), only 0.52 eV (Li<sub>2</sub>S<sub>4</sub>), 0.45 eV (Li<sub>2</sub>S<sub>6</sub>), and 0.42 eV (Li<sub>2</sub>S<sub>8</sub>), respectively. From the binding geometries in Figure S4, it can be seen that the LiPSs on the carbon surface were relaxed without obvious bonding cooperation. According to the reports of Zhang and Nazar et al., the weak interaction might be due to the van der Waals forces between molecules [14,15]. The different affinities of NiCo<sub>2</sub>O<sub>4</sub> and carbon for LiPSs were reflected in the visual adsorption experiment (Figure 3c). After adding NiCo<sub>2</sub>O<sub>4</sub> to the solution, it could be clearly observed that the color of the Li<sub>2</sub>S<sub>4</sub> solution changed from brown to colorless. For activated carbon of the same mass, the color hardly changed at all. The strong adsorption of LiPSs by the former would contribute to the inhibition of the shuttle effect in the NiCo<sub>2</sub>O<sub>4</sub>@PP system.

Figures 3d,e and S5 reveal the X-ray photoelectron spectroscopy (XPS) results of NiCo<sub>2</sub>O<sub>4</sub> before and after interacting with Li<sub>2</sub>S<sub>4</sub>. The XPS survey spectra (from 0 to 1300 eV) in Figure S5 show that only the sulfur element changed before and after LiPS adsorption, indicating that no other impurities were involved in the reaction. In detail, for the pure NiCo<sub>2</sub>O<sub>4</sub> sample, the Co 2p<sub>3/2</sub> spectrum exhibited a broad peak consisting of two spin-orbit doublets, which corresponded to Co<sup>2+</sup> and Co<sup>3+</sup> [30,31]. The Co 2p<sub>3/2</sub> spectrum were also fitted in a similar way. Two components at about 855.5 eV and 835.8 eV corresponded to Ni<sup>3+</sup> and Ni<sup>2+</sup>, respectively. The wide peaks between 360 and 362 eV in binding energy were the corresponding satellite peaks [23]. After the adsorption of Li<sub>2</sub>S<sub>4</sub>, all the characteristic peaks shifted toward a lower binding energy, meaning that the Ni and Co cations interacted strongly with LiPSs, which was consistent with the results of previous studies [32–35]. In addition, the reduction in the Ni<sup>3+</sup> and Co<sup>3+</sup> contents suggested a partial reduction in the oxidation states of Ni and Co, which might be attributed to the charge transfer from S<sub>4</sub><sup>2−</sup> [34].

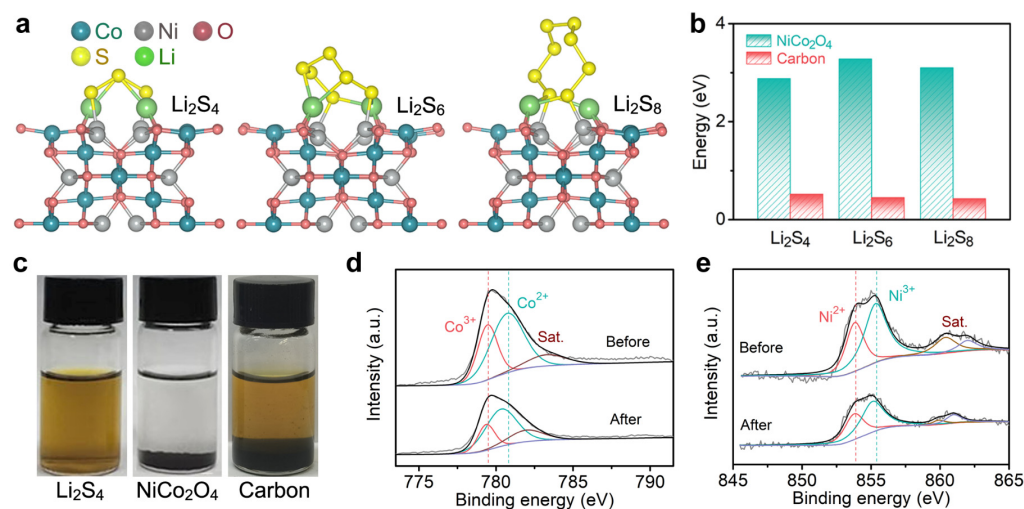


**Figure 3.** (a) Mechanism diagram of interaction between NiCo<sub>2</sub>O<sub>4</sub> and LiPSs. (b) The corresponding adsorption energies. (c) Visual adsorption of Li<sub>2</sub>S<sub>4</sub>. (d) Co 2p and (e) Ni 2p XPS results of NiCo<sub>2</sub>O<sub>4</sub> before and after Li<sub>2</sub>S<sub>4</sub> adsorption.

Subsequently, using the Li metal as the anode, the effect of the NiCo<sub>2</sub>O<sub>4</sub>@PP composite separator on the dynamics of a Li–S battery system was tested. Cyclic voltammetry (CV) curves of the carbon nanotube base sulfur cathodes with primitive PP or a NiCo<sub>2</sub>O<sub>4</sub>@PP separator conducted in a potential window of 1.7–2.6 V are presented in Figure 4a. Both cells exhibited classic LiPS electrochemical reaction characteristics. The absence of other peaks indicated that the electrode process was derived from the reaction with lithium and sulfur. Two cathode peaks could be attributed to the formation of soluble long-chain LiPSs and solid short-chain Li<sub>2</sub>S<sub>2</sub>/Li<sub>2</sub>S by sulfur reduction, respectively. The wide anode peak at about 2.3–2.4 V represented the oxidation of Li<sub>2</sub>S<sub>2</sub>/Li<sub>2</sub>S to S<sub>8</sub> [36]. The voltage polarization of the cell using the NiCo<sub>2</sub>O<sub>4</sub>@PP composite separator was low, and the potential difference between the cathode peak and the anode peak was only 0.299 V. However, the cathode system with the initial PP separator was as high as 0.337 V, indicating that NiCo<sub>2</sub>O<sub>4</sub> promoted the redox kinetics of the LiPS electrochemical system [37]. Figure 4b,c shows the Tafel plots and fitted slope values for the oxidation and the second reduction peaks in the CV curves in Figure 4a, respectively. Slopes as low as 85 and 107 mV dec<sup>−1</sup> implied that the NiCo<sub>2</sub>O<sub>4</sub> system had a better LiPSs conversion rate, which might be due to catalytic behavior at active sites rich in Ni and Co [38,39]. In this case, the accumulation of LiPSs would be avoided [34,40].

Figure 4d reveals the charge–discharge plots of different separator systems at 0.2 C. A higher reversible capacity of 1386 mAh g<sup>−1</sup> was reached by the NiCo<sub>2</sub>O<sub>4</sub>@PP electrode. The voltage difference (peak spacing,  $\Delta E$ ) of NiCo<sub>2</sub>O<sub>4</sub>@PP was 0.165 V, lower than that of the PP electrode (0.196 V), which was consistent with the results of the CV. This might be due to the large number of active sites NiCo<sub>2</sub>O<sub>4</sub> provides for the catalytic conversion of polysulfides [33,35]. From the CV and Tafel slope results, it can be seen that the NiCo<sub>2</sub>O<sub>4</sub>@PP had a relatively lower electrode process obstacle, faster charge/electron transfer rate, and better catalytic performance and redox kinetics. Therefore, in the charge–discharge view, it exhibited a low redox potential. Meanwhile, in the charging process, the initial overpotential of the pure PP system was slightly higher than that of NiCo<sub>2</sub>O<sub>4</sub>@PP (Figure 4e), indicating that the energy barrier of Li<sub>2</sub>S<sub>2</sub>/Li<sub>2</sub>S decomposition in the later system was low [41]. Electrochemical impedance spectroscopy (EIS) in Figure 4f (10 mHz–100 kHz) showed a small NiCo<sub>2</sub>O<sub>4</sub>@PP semicircle, which suggests that its charge-transfer resistance ( $R_{ct}$ ) was lower than the PP electrode. Here, the semicircle in the high frequency region corresponded to the charge-transfer step, while the straight line in the low frequency region corresponded to ion diffusion. After fitting (inset of Figure 4f) and calculation, the  $R_{ct}$  of the NiCo<sub>2</sub>O<sub>4</sub>@PP electrode was ~14.6 ohm, while the original PP electrode was ~29.5 ohm.

In addition, the surface resistance ( $R_{surf}$ ) of the former was only  $\sim 7.1$  ohm, while the later was  $\sim 12.1$  ohm. All of these electrochemical properties indicate that the  $\text{NiCo}_2\text{O}_4$  modified layer had an excellent promotion effect on the reaction kinetics of the cell.

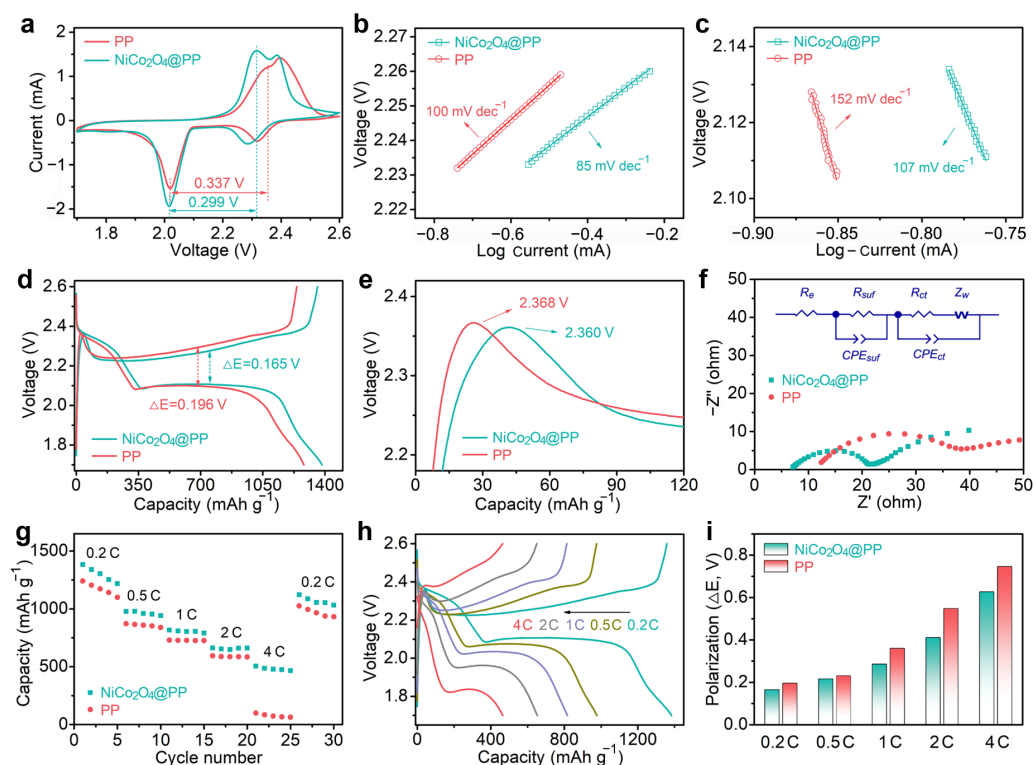


**Figure 4.** (a) The CV curves with pure PP and modified separators at  $0.1 \text{ mV s}^{-1}$ . (b,c) Corresponding Tafel results and fitted slope values. (d,e) Comparison of the charge–discharge plots at  $0.2 \text{ C}$ , and the corresponding initial process of the charge details. (f) EIS spectra. The inset is the corresponding equivalent circuit.  $R_e$  is the electrolyte resistance.  $R_{surf}$  is the surface resistance.  $R_{ct}$  is the charge transfer resistance.  $Z_w$  is the Warburg impedance. The constant phase element (CPE) was used to compensate for the non-ideal behavior of the electrode. (g,h) Rate performance and charge–discharge curves at different currents. (i) Comparison of the potential polarizations of different separators.

In terms of battery performance, the above dynamic improvement was manifested in the rapid charging–discharging ability. Figure 4g shows the comparison of the rate. At  $0.2 \text{ C}$ ,  $0.5 \text{ C}$ ,  $1 \text{ C}$ ,  $2 \text{ C}$ , and  $4 \text{ C}$ , the discharge capacities of the  $\text{NiCo}_2\text{O}_4$ @PP-based cell were 1386, 982, 821, 656, and 505  $\text{mAh g}^{-1}$ , respectively, while the pure PP electrode was only 1246, 876, 731, 583, and 102  $\text{mAh g}^{-1}$ . The retention of the electrode capacity at high rate (such as  $4 \text{ C}$ ) indicated that the  $\text{NiCo}_2\text{O}_4$  coating could support the rapid charging–discharging of the cell. Meanwhile, when the current density returned to  $0.2 \text{ C}$ , the former still reached  $1122 \text{ mAh g}^{-1}$ , higher than that of the PP electrode ( $1011 \text{ mAh g}^{-1}$ ). Figure 4h displays the corresponding charging–discharging profiles at various rates. It could be seen that it retained the platform characteristics of LiPS reactions, especially at the high magnification of  $4 \text{ C}$ . Apart from that, although the polarization degree of the battery increased with the increase in the current density, the  $\text{NiCo}_2\text{O}_4$ @PP electrode always maintained a low voltage polarization, suggesting that the as-obtained  $\text{NiCo}_2\text{O}_4$  effectively improved the cathode dynamics (Figure 4i), which was consistent with the data of CV and EIS. For the pure PP separator, the large polarization meant that the execution of the LiPS reaction at this rate was difficult [42,43].

Finally, to verify the improvement in the stability of the as-assembled Li–S cell by the  $\text{NiCo}_2\text{O}_4$  modified separator, that is, the inhibition effect of the shuttle effect, various charge–discharge cycle experiments were conducted in Figure 5. At  $0.5 \text{ C}$ , the  $\text{NiCo}_2\text{O}_4$ @PP-based Li–S cell retained a considerable capacity of  $702 \text{ mAh g}^{-1}$  over 100 cycles (Figure 5a). The

Coulombic efficiency gradually increased to  $\sim 100\%$  in the first five cycles and remained at  $\sim 99.3\%$  at the 100th. In the initial phase of the cyclic stability experiment, there was a gradual increase in capacity. This might be due to the low capacity caused by insufficient activation of the active substance at the beginning of cell operation. After a period of activation, the electrolyte was fully immersed into the cathode, and the sulfur was transformed from the initial status to a more electrochemically stable state. As a result, the electrodes exhibited high capacity [44,45]. Therefore, the cell capacity gradually reached its maximum. For the PP system, the capacity was only  $501 \text{ mAh g}^{-1}$  after 100 cycles. Impressively, when the current density was increased to 4 C, the former could run stably for more than 300 turns. As shown in Figure 5c, it could get up to a whopping  $505 \text{ mAh g}^{-1}$  capacity after activation. After 300 cycles, the capacity attenuation of each cycle of the Li-S cell with the  $\text{NiCo}_2\text{O}_4/\text{PP}$  separator was only  $\sim 0.064\%$ . The Coulombic efficiency was stable around  $99.4\%$ . More importantly, the charge–discharge curve in Figure S6 during the above cycling remained a good redox platform, showing excellent cyclic stability.

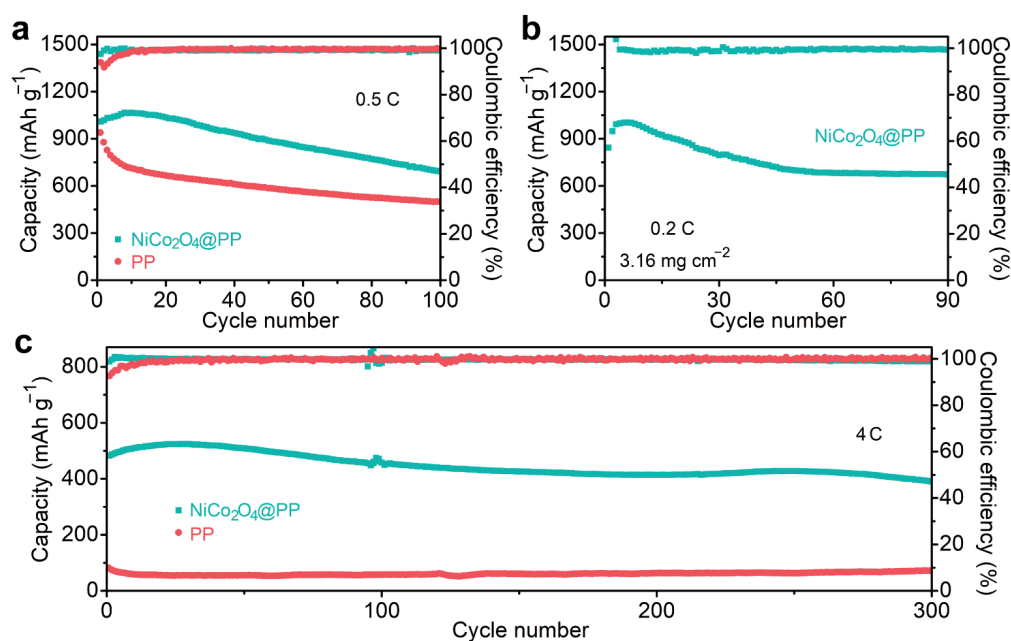


**Figure 5.** (a) Cyclic properties of the sulfur cathodes with different separators at 0.5 C. (b) High loading performance at 0.2 C. (c) High rate and long cycle comparison.

In addition to the rate and stability, the high sulfur loading is another important criterion of the Li-S cell [46,47]. Figure 5c exhibits the cycling performance of the  $\text{NiCo}_2\text{O}_4/\text{PP}$ -based cathode at a high sulfur loading of  $3.16 \text{ mg cm}^{-2}$ . The maximum area capacity of about  $3.2 \text{ mAh cm}^{-2}$  ( $1012 \text{ mAh g}^{-1}$ , 0.2 C) was obtained and maintained at about  $2.2 \text{ mAh cm}^{-2}$  in subsequent cycles. The excellent electrochemical performance was not only due to the adsorption and blocking of LiPSs by the  $\text{NiCo}_2\text{O}_4$  hollow nanospheres, but also due to the enhancement of redox reaction kinetics in the battery system by the abundant active catalytic sites provided by the huge specific surface area. Subsequently, the cell was disassembled after the cyclic stability test, and the composite separator was characterized by SEM. As shown in Figure S7, after long-term charge and discharge cycling, disassembly and cleaning, the surface of the modified separator was still covered with a large amount of  $\text{NiCo}_2\text{O}_4$  matrix composite material, indicating that the obtained composite membrane showed excellent mechanical stability.

### 3. Materials and Methods

#### 3.1. Preparation of Hollow $\text{NiCo}_2\text{O}_4$ and Modified Separator

For the carbon nanosphere templates, 10 g of glucose was dissolved in 40 mL deionized water to form a clarified solution. After 6 h of hydrothermal reaction at  $160^\circ\text{C}$ , the reactor

was cooled naturally. The brown precipitates were washed with water and ethanol three times, centrifuged, and dried in vacuum.

Subsequently, in the synthesis of hollow NiCo<sub>2</sub>O<sub>4</sub> nanospheres, about 50 mg of the carbon nanospheres prepared above were dispersed ultrasonically in a mixture of 40 mL deionized water and 20 mL ethanol. A total of 0.29 g of Ni(NO<sub>3</sub>)<sub>2</sub>•6H<sub>2</sub>O, 0.582 g of Co(NO<sub>3</sub>)<sub>2</sub>•9H<sub>2</sub>O and 6 mmol of urea (0.36 g) were added and stirred for 1 hour. After 6 h of reaction in the water bath at 80 °C, it was cooled to room temperature. The precursors were separated by centrifugation, washed with deionized water and ethanol, respectively, and dried at 80 °C. Finally, the dried powder was calcined in air at 350 °C for 2 h with 0.5 °C min<sup>-1</sup> to obtain the hollow NiCo<sub>2</sub>O<sub>4</sub> product.

For a NiCo<sub>2</sub>O<sub>4</sub>@PP separator. The slurry consisting of NiCo<sub>2</sub>O<sub>4</sub>, polyvinylidene fluoride (PVDF) binder, and a carbon nanotube conductive agent with a weight ratio of 7:2:1 was coated on one side of a commercial Celgard-2400 PP separator. Then, the as-obtained modified separator was dried under vacuum.

### 3.2. Materials Characterization

The SEM and TEM (including HRTEM) images were carried out with a Hitachi Regulus 8100 and FEI Tecnai G<sup>2</sup> 20, respectively. The XRD pattern was observed on a Rigaku D/Max III diffractometer with Cu K $\alpha$  radiation ( $\lambda = 1.5418 \text{ \AA}$ ). The specific surface area and pore size distribution were measured with a Kubo-X1000 analyzer with the BET calculation. The contact angle test was completed by JY-82B Kruss DSA. The XPS results were obtained using a Thermo Scientific K-Alpha tester. TGA was performed using a NETZSCH ASAP2020 thermal analyzer under the protection of air gas.

### 3.3. Visualization Li<sub>2</sub>S<sub>4</sub> Adsorption

Briefly, sulfur and Li<sub>2</sub>S with a molar ratio of 3:1 was added to a mixed solution of 1,3-dioxolane (DOL) and 1,2-dimethoxymethane (DME) at 50 °C with stirring. The Li<sub>2</sub>S<sub>4</sub> solution concentration was controlled at about 0.5 M. The same mass of carbon nanotubes and hollow NiCo<sub>2</sub>O<sub>4</sub> nanospheres were added to the above solution, respectively.

### 3.4. Electrochemical Measurements

The sulfur composite cathode was prepared by melting sublimated sulfur power (70 wt%) and carbon nanotubes (30 wt%) at 155 °C in an airtight reactor. The resulting sulfur-based composite was then mixed with acetylene black and PVDF in a N-methylpyrrolidone (NMP) solvent at a mass ratio of 7:2:1 and evenly coated on clean Al foil. For the general tests, the sulfur loading was controlled at about 1 mg cm<sup>-2</sup>. For the high loading tests, the sulfur loading was 3.16 mg cm<sup>-2</sup>. Subsequently, Li-S cells (CR2032) were assembled in a glove box filled with Ar. Lithium foil and pure PP or NiCo<sub>2</sub>O<sub>4</sub>@PP were used as the anode and separator, respectively. The DOL/DME (v/v, 1:1) solvent with 1 M lithium (trifluoromethylsulfonyl) imide (LiTFSI) and 0.1 M LiNO<sub>3</sub> was used as the electrolyte. The removal of the battery all took place in the glove box and the separator sample was cleaned with DME.

All constant-current charge–discharge tests were performed on a LAND system with a voltage range of 1.7–2.6 V. The CV and EIS were tested on an electrochemical workstation (CHI 660E).

### 3.5. Theoretical Calculation

All theoretical calculations were conducted using the DMol<sup>3</sup> system. Density functional theory was used to calculate the LiPS adsorption on the NiCo<sub>2</sub>O<sub>4</sub> matrix. The Perdew–Burke–Ernzerhof form of the exchange–correlation effects was employed. Monkhorst–Pack mesh k-points were used to sample the Brillouin zone with a cut-off energy of 300 eV. The binding energy ( $E_b$ ) can be calculated as  $E_b = E_{\text{sub}} + E_{\text{ps}} - E_{\text{sub+ps}}$ , where  $E_{\text{sub}}$ ,  $E_{\text{ps}}$ , and  $E_{\text{sub+ps}}$  represent the ground-state energies of the substrate, polysulfide, and substrate-polysulfide, respectively.

#### 4. Conclusions

In summary, the edelweiss shaped hollow nanospheres assembled by ultra-thin NiCo<sub>2</sub>O<sub>4</sub> nanosheets were prepared by a simple template method. The specific surface area of the product was up to ~281 m<sup>2</sup> g<sup>-1</sup> due to the hollow inner cavity and the surface nanosheet structure. This provided a wealth of active sites for the anchoring and catalytic conversion of LiPSs. As the modification layer of the separator, the prepared NiCo<sub>2</sub>O<sub>4</sub> nanostructures not only physically hindered the diffusion of LiPSs and limited their electrochemical reaction, but also chemically interacted with LiPSs and the electrolyte and promoted the reaction kinetics of the electrode. As a result, the Li-S cell with the NiCo<sub>2</sub>O<sub>4</sub>@PP separator exhibited an amazing capacity of 1386 mAh g<sup>-1</sup> at 0.2 C and a high capacity of 505 mAh g<sup>-1</sup> at 4 C. Even after 300 cycles, it still had a commendable capacity retention of ~80.6%. Generally, we demonstrated a multifunctional NiCo<sub>2</sub>O<sub>4</sub>@PP composite separator that enabled a Li-S battery with high capacity, good rate, and stable cycling life.

**Supplementary Materials:** The following supporting information can be downloaded at: <https://www.mdpi.com/article/10.3390/molecules28041539/s1>, Figure S1: SEM images of (a) carbon sphere templates and (b) Co-Ni precursors; Figure S2. TGA results of (a) pure carbon sphere, and (b) precursor composite; Figure S3. Elemental mapping of NiCo<sub>2</sub>O<sub>4</sub>: (a) SEM, (b) TEM; Figure S4. Mechanism diagram of interaction between carbon and LiPSs; Figure S5. XPS survey spectra of NiCo<sub>2</sub>O<sub>4</sub> before and after Li<sub>2</sub>S<sub>4</sub> adsorption; Figure S6. Discharge-charge profiles of NiCo<sub>2</sub>O<sub>4</sub>@PP cathode at different cycles; Figure S7. The surface SEM of composite separator after cyclic test.

**Author Contributions:** Conceptualization, J.P. and X.Z.; Methodology, X.Z.; Software, X.Z.; Validation, J.P., S.Y. and X.Z.; Formal analysis, S.Y.; Investigation, J.P.; Resources, J.P.; Data curation, X.Z.; Writing—original draft preparation, J.P.; Writing—review and editing, J.P. and X.Z.; Visualization, X.Z.; Supervision, J.W. and S.Y.; Project administration, J.P.; Funding acquisition, J.P. All authors have read and agreed to the published version of the manuscript.

**Funding:** This research was funded by the National Natural Science Foundation of China (grant number 52207227) and the Doctoral Research Initiation Foundation of Anhui Normal University (grant number 751973).

**Institutional Review Board Statement:** Not applicable.

**Informed Consent Statement:** Not applicable.

**Data Availability Statement:** Not applicable.

**Acknowledgments:** This research was supported in part by the National Natural Science Foundation of China, the Doctoral Research Initiation Foundation of Anhui Normal University. The theoretical calculations were conducted at the computing facilities in the High-Performance Computing Center of Nanjing University.

**Conflicts of Interest:** The authors declare no conflict of interest.

**Sample Availability:** Samples of the compounds are available from the authors.

#### References

1. Yoshie, Y.; Hori, K.; Mae, T.; Noda, S. High-energy-density Li-S battery with positive electrode of lithium polysulfides held by carbon nanotube sponge. *Carbon* **2021**, *182*, 32–41. [[CrossRef](#)]
2. Liu, Y.; Elias, Y.; Meng, J.S.; Aurbach, D.; Zou, R.; Xia, D.; Pang, Q. Electrolyte solutions design for lithium-sulfur batteries. *Joule* **2021**, *5*, 2323–2364. [[CrossRef](#)]
3. Yao, W.; Zheng, W.; Xu, J.; Tian, C.; Han, K.; Sun, W.; Xiao, S. ZnS-SnS@NC Heterostructure as robust lithiophilicity and sulfiphilicity mediator toward high-rate and long-life lithium-sulfur batteries. *ACS Nano* **2021**, *15*, 7114–7130. [[CrossRef](#)]
4. Ren, W.; Ma, W.; Zhang, S.; Tang, B. Recent advances in shuttle effect inhibition for lithium sulfur batteries. *Energy Storage Mater.* **2019**, *23*, 707–732. [[CrossRef](#)]
5. Lakshmi, K.; Vedhanarayanan, B.; Shen, H.; Lin, T. Encapsulating chalcogens as the rate accelerator into MoS<sub>2</sub> with expanded interlayer spacing to boost the capacity and cycle stability of Li-S batteries. *2D Mater.* **2022**, *9*, 034002. [[CrossRef](#)]
6. Donato, G.D.; Ates, T.; Adenusi, H.; Varzi, A.; Navarra, M.A.; Passerini, S. Electrolyte Measures to Prevent Polysulfide Shuttle in Lithium-Sulfur Batteries. *Batter. Supercaps* **2022**, *5*, e202200097. [[CrossRef](#)]

7. Pu, J.; Gong, W.; Shen, Z.; Wang, L.; Yao, Y.; Hong, G. CoNiO<sub>2</sub>/Co<sub>4</sub>N Heterostructure nanowires assisted polysulfide reaction kinetics for improved lithium-sulfur batteries. *Adv. Sci.* **2022**, *9*, 2104375. [[CrossRef](#)] [[PubMed](#)]
8. Huang, S.; Wang, Z.; Lim, Y.V.; Wang, Y.; Li, Y.; Zhang, D.; Yang, H. Recent advances in heterostructure engineering for lithium-sulfur batteries. *Adv. Energy Mater.* **2021**, *11*, 2003689. [[CrossRef](#)]
9. Zhai, P.; Peng, H.; Cheng, X.; Zhu, L.; Huang, J.; Zhu, W.; Zhang, Q. Scaled-up fabrication of porous-graphene-modified separator for high-capacity lithium-sulfur batteries. *Energy Storage Mater.* **2017**, *7*, 56–63. [[CrossRef](#)]
10. Pu, J.; Wang, T.; Zhu, X.; Tan, Y.; Gao, L.; Chen, J.; Huang, J.; Wang, Z. Multifunctional Ni/NiO heterostructure nanoparticles doped carbon nanorods modified separator for enhancing Li-S battery performance. *Electrochim. Acta* **2022**, *435*, 141396. [[CrossRef](#)]
11. Lee, D.K.; Ahn, C.W.; Jeon, H.-J. Web-structured graphitic carbon fiber felt as an interlayer for rechargeable lithium-sulfur batteries with highly improved cycling performance. *J. Power Sources* **2017**, *360*, 559–568. [[CrossRef](#)]
12. Ma, Z.; Jing, F.; Li, J.; Zhao, Y.; Shao, G. High electrical conductivity of 3D mesoporous carbon nanocage as an efficient polysulfide buffer layer for high sulfur utilization in lithium-sulfur batteries. *J. Mater. Chem. A* **2019**, *7*, 789, 71–79. [[CrossRef](#)]
13. Yanilmaz, M.; Asiri, A.M.; Zhang, X. Centrifugally spun porous carbon microfibers as interlayer for Li-S batteries. *J. Mater. Sci.* **2020**, *55*, 3538–3548. [[CrossRef](#)]
14. Yuan, Z.; Peng, H.; Hou, T.; Huang, J.; Chen, C.; Wang, D.; Cheng, X.; Wei, F.; Zhang, Q. Powering Lithium-Sulfur Battery Performance by Propelling Polysulfide Redox at Sulfiphilic Hosts. *Nano Lett.* **2016**, *16*, 519–527. [[CrossRef](#)] [[PubMed](#)]
15. Pang, Q.; Kundu, D.; Nazar, L.F. A graphene-like metallic cathode host for long-life and high-loading lithium-sulfur batteries. *Mater. Horiz.* **2016**, *3*, 130–136. [[CrossRef](#)]
16. Kong, W.; Yan, L.; Luo, Y.; Wang, D.; Jiang, K.; Li, Q.; Fan, S.; Wang, J. Ultrathin MnO<sub>2</sub>/Graphene Oxide/Carbon Nanotube Interlayer as Efficient Polysulfide-Trapping Shield for High-Performance Li-S Batteries. *Adv. Funct. Mater.* **2017**, *27*, 1606663. [[CrossRef](#)]
17. Zheng, C.; Niu, S.; Lv, W.; Zhou, G.; Li, J.; Fan, S.; Deng, Y.; Pan, Z.; Li, B.; Kang, F.; et al. Propelling polysulfides transformation for high-rate and long-life lithium-sulfur batteries. *Nano Energy* **2017**, *33*, 306–312. [[CrossRef](#)]
18. Wang, J.; Liang, J.; Wu, J.; Xuan, C.; Wu, Z.; Guo, X.; Lai, C.; Zhu, Y.; Wang, D. Coordination effect of network NiO nanosheet and a carbon layer on the cathode side in constructing a high-performance lithium-sulfur battery. *J. Mater. Chem. A* **2018**, *6*, 6503–6509. [[CrossRef](#)]
19. Pu, J.; Tan, Y.; Wang, T.; Zhu, X.; Fan, S. Ultrathin Two-Dimensional Fe-Co Bimetallic Oxide Nanosheets for Separator Modification of Lithium-Sulfur Batteries. *Molecules* **2022**, *27*, 7762. [[CrossRef](#)]
20. Pu, J.; Liu, Z.; Ma, Z.; Wang, J.; Zhang, L.; Chang, S.; Wu, W.; Shen, Z.; Zhang, H. Structure design of NiCo<sub>2</sub>O<sub>4</sub> electrodes for high performance pseudocapacitors and lithium-ion batteries. *J. Mater. Chem. A* **2016**, *4*, 17394–17402. [[CrossRef](#)]
21. Sun, X.; Li, Y. Colloidal Carbon Spheres and Their Core/Shell Structures with Noble-Metal Nanoparticles. *Angew. Chem. Int. Ed.* **2004**, *43*, 597–601. [[CrossRef](#)] [[PubMed](#)]
22. Pu, J.; Wang, J.; Jin, X.; Cui, F.; Sheng, E.; Wang, Z. Porous hexagonal NiCo<sub>2</sub>O<sub>4</sub> nanoplates as electrode materials for supercapacitors. *Electrochim. Acta* **2013**, *106*, 226–234. [[CrossRef](#)]
23. Pu, J.; Jin, X.; Wang, J.; Cui, F.; Chu, S.; Sheng, E.; Wang, Z. Shape-controlled synthesis of ternary nickel cobaltite and their application in supercapacitors. *J. Electronal. Chem.* **2013**, *707*, 66–73. [[CrossRef](#)]
24. Gu, W.; Pan, Z.; Tao, H.; Guo, P.J.; Zhong, C.; Li, J.; Ye, C.; Zhou, Q. Boron-modulated surface of hollow nickel framework for improved hydrogen evolution. *Chem. Commun.* **2021**, *57*, 2404–2407. [[CrossRef](#)] [[PubMed](#)]
25. Pan, X.; Zhu, K.; Gong, W.; Pu, J.; Li, X.; Guo, C.; Wu, L.; Wang, R.; Li, H.; Sun, J.; et al. “One Stone Two Birds” Design for Dual-Functional TiO<sub>2</sub>-TiN Heterostructures Enabled Dendrite-Free and Kinetics-Enhanced Lithium-Sulfur Batteries. *Adv. Energy Mater.* **2022**, *12*, 2200308.
26. Yim, T.; Han, S.H.; Park, N.H.; Park, M.-S.; Lee, J.H.; Shin, J.; Choi, J.W.; Jung, Y.; Jo, Y.N.; Yu, J.-S.; et al. Effective Polysulfide Rejection by Dipole-Aligned BaTiO<sub>3</sub> Coated Separator in Lithium-Sulfur Batteries. *Adv. Funct. Mater.* **2016**, *26*, 7817–7823. [[CrossRef](#)]
27. He, J.; Chen, Y.; Manthiram, A. Vertical Co<sub>9</sub>S<sub>8</sub> hollow nanowall arrays grown on a Celgard separator as a multifunctional polysulfide barrier for high-performance Li-S batteries. *Energy Environ. Sci.* **2018**, *11*, 2560–2568. [[CrossRef](#)]
28. Zhang, Q.; Wang, Y.; Seh, Z.W.; Fu, Z.; Zhang, R.; Cui, Y. Understanding the anchoring effect of two-dimensional layered materials for lithium-sulfur batteries. *Nano Lett.* **2015**, *15*, 3780–3786. [[CrossRef](#)]
29. Li, H.; Gu, S.; Tao, B.; Xie, Y.; Guo, F.; Zhang, S.; Liu, B.; Liu, J.; Zhang, W.; Chang, H. Highly wrinkled NiO nanosheet-based hierarchical structure/reduced fluorographene composite for enhanced performance of lithium-sulfur battery. *J. Taiwan Inst. Chem. E.* **2020**, *111*, 205–211. [[CrossRef](#)]
30. Zhong, Y.; Yin, L.; He, P.; Liu, W.; Wu, Z.; Wang, H. Surface Chemistry in Cobalt Phosphide-Stabilized Lithium-Sulfur Batteries. *J. Am. Chem. Soc.* **2018**, *140*, 1455–1459. [[CrossRef](#)]
31. Niu, X.; Wang, X.; Wang, D.; Li, Y.; Zhang, Y.; Zhang, Y.; Yang, T.; Yu, T.; Tu, J. Metal hydroxide—a new stabilizer for the construction of sulfur/carbon composites as high performance cathode materials for lithium-sulfur batteries. *J. Mater. Chem. A* **2015**, *3*, 17106–17112. [[CrossRef](#)]

32. Liang, X.; Kwok, C.Y.; Lodi-Marzano, F.; Pang, Q.; Cuisinier, M.; Huang, H.; Hart, C.J.; Houtarde, D.; Kaup, K.; Sommer, H.; et al. Tuning Transition Metal Oxide-Sulfur Interactions for Long Life Lithium Sulfur Batteries: The “Goldilocks” Principle. *Adv. Energy Mater.* **2016**, *6*, 1501636. [[CrossRef](#)]
33. Chen, S.; Zhang, J.; Wang, Z.; Nie, L.; Hu, X.; Yu, Y.; Liu, W. Electrocatalytic NiCo<sub>2</sub>O<sub>4</sub> Nanofiber Arrays on Carbon Cloth for Flexible and High-Loading Lithium–Sulfur Batteries. *Nano Lett.* **2021**, *21*, 5285–5292. [[CrossRef](#)]
34. Liu, Y.; Han, D.; Wang, L.; Li, G.; Liu, S.; Gao, X. NiCo<sub>2</sub>O<sub>4</sub> Nanofibers as Carbon-Free Sulfur Immobilizer to Fabricate Sulfur-Based Composite with High Volumetric Capacity for Lithium–Sulfur Battery. *Adv. Energy Mater.* **2019**, *9*, 1803477. [[CrossRef](#)]
35. Luo, D.; Deng, Y.; Zhang, Z.; Li, J.; Liang, R.; Li, M.; Jiang, Y.; Zhang, W.; Liu, Y.; Lei, W.; et al. Synergistic Engineering of Defects and Architecture in Binary Metal Chalcogenide toward Fast and Reliable Lithium–Sulfur Batteries. *Adv. Energy Mater.* **2019**, *9*, 1900228. [[CrossRef](#)]
36. Hu, L.; Dai, C.; Liu, H.; Li, Y.; Shen, B.; Chen, Y.; Bao, S.; Xu, M. Double-Shelled NiO–NiCo<sub>2</sub>O<sub>4</sub> Heterostructure@Carbon Hollow Nanocages as an Efficient Sulfur Host for Advanced Lithium–Sulfur Batteries. *Adv. Energy Mater.* **2018**, *8*, 1800709. [[CrossRef](#)]
37. Lei, T.; Chen, W.; Lv, W.; Huang, J.; Zhu, J.; Chu, J.; Yan, C.; Wu, C.; Yan, Y.; He, W.; et al. Inhibiting Polysulfide Shuttling with a Graphene Composite Separator for Highly Robust Lithium–Sulfur Batteries. *Joule* **2018**, *2*, 2091–2104. [[CrossRef](#)]
38. Wu, Q.; Zhou, X.; Xu, J.; Cao, F.; Li, C. Adenine Derivative Host with Interlaced 2D Structure and Dual Lithiophilic–Sulfiphilic Sites to Enable High-Loading Li–S Batteries. *ACS Nano* **2019**, *13*, 9520–9532. [[CrossRef](#)] [[PubMed](#)]
39. Chen, Y.; Ji, X. Bamboo-like Co<sub>3</sub>O<sub>4</sub> nanofiber as host materials for enhanced lithium-sulfur battery performance. *J. Alloys Compound.* **2019**, *777*, 688–692. [[CrossRef](#)]
40. Pu, J.; Wang, Z.; Xue, P.; Zhu, K.; Li, J.; Yao, Y. The effect of NiO–Ni<sub>3</sub>N interfaces in in-situ formed heterostructure ultrafine nanoparticles on enhanced polysulfide regulation in lithium-sulfur batteries. *J. Energy Chem.* **2022**, *68*, 762–770. [[CrossRef](#)]
41. Ye, Z.; Jiang, Y.; Feng, T.; Wang, Z.; Li, L.; Wu, F.; Chen, R. Curbing poly-sulfide shuttling by synergistic engineering layer composed of supported Sn<sub>4</sub>P<sub>3</sub> nanodots electrocatalyst in lithium-sulfur batteries. *Nano Energy* **2020**, *70*, 104532. [[CrossRef](#)]
42. Wang, R.; Yuan, Y.; Zhang, J.; Zhong, X.; Liu, J.; Xie, Y.; Zhong, S.; Xu, Z. Embedding Fe<sub>2</sub>P nanocrystals in bayberry-like N, P-enriched carbon nanospheres as excellent oxygen reduction electrocatalyst for zinc-air battery. *J. Power Sources* **2021**, *501*, 230006. [[CrossRef](#)]
43. Xiong, D.; Huang, S.; Fang, D.; Yan, D.; Li, G.; Yan, Y.; Chen, S.; Liu, Y.; Li, X.; Lim, Y.V.; et al. Porosity Engineering of MXene Membrane towards Polysulfide Inhibition and Fast Lithium Ion Transportation for Lithium-Sulfur Batteries. *Small* **2021**, *17*, 2007442. [[CrossRef](#)] [[PubMed](#)]
44. Cui, Z.; Zu, C.; Zhou, W.; Manthiram, A.; Goodenough, J.B. Mesoporous Titanium Nitride-Enabled Highly Stable Lithium-Sulfur Batteries. *Adv. Mater.* **2016**, *28*, 6926–6931. [[CrossRef](#)]
45. Zhang, J.; You, C.; Zhang, W.; Wang, J.; Guo, S.; Xu, Y. Conductive bridging effect of TiN nanoparticles on the electrochemical performance of TiN@CNT-S composite cathode. *Electrochim. Acta* **2017**, *250*, 159–166. [[CrossRef](#)]
46. Wei, C.; Tian, M.; Wang, M.; Shi, Z.; Yu, L.; Li, S.; Fan, Z.; Yang, R.; Sun, J. Universal in Situ Crafted MO<sub>x</sub>-MXene Heterostructures as Heavy and Multifunctional Hosts for 3D-Printed Li–S Batteries. *ACS Nano* **2020**, *14*, 16073–16084. [[CrossRef](#)]
47. Zhang, Y.; Wang, B.; Jing, P.; Guo, Y.; Zhang, Y.; Wei, Y.; Wang, Q.; Zhang, Y.; Wu, H. Bioderived carbon fiber conductive networks with inlaid electrocatalysts as an ultralight freestanding interlayer for working LiSeS<sub>2</sub> pouch cells. *Carbon* **2022**, *189*, 10–20. [[CrossRef](#)]

**Disclaimer/Publisher’s Note:** The statements, opinions and data contained in all publications are solely those of the individual author(s) and contributor(s) and not of MDPI and/or the editor(s). MDPI and/or the editor(s) disclaim responsibility for any injury to people or property resulting from any ideas, methods, instructions or products referred to in the content.